Applied Ocean Research 65 (2017) 251–261

Contents lists available at ScienceDirect

Applied Ocean Research

journal homepage: www.elsevier.com/locate/apor

A task-based hierarchical control strategy for autonomous motion of an unmanned surface vehicle swarm

Zihe Qin, Zhuang Lin*, Dongmei Yang, Ping Li

College of Shipbuilding Engineering, Harbin Engineering University, Harbin, China

ARTICLE INFO

Article history:
Received 12 October 2016
Received in revised form 12 April 2017
Accepted 19 April 2017
Available online 4 May 2017

Keywords:
USV
Swarm control
Potential function
Sliding-mode
Underactuated

ABSTRACT

In this paper, a hierarchical control framework with relevant algorithms is proposed to achieve autonomous navigation for an underactuated unmanned surface vehicle (USV) swarm. In order to implement automatic target tracking, obstacle avoidance and avoid collisions between group members, the control framework is divided into three layers based on task assignments: flocking strategy design, motion planning and control input design. The flocking strategy design transmits some basic orders to swarm members. Motion planning applies the potential function method and then improves it; thus, the issue of autonomous control is transformed into one of designing the velocity vector. In the last layer, the control inputs (surge force and yaw moment) are designed using the sliding mode method, and the problem of underactuation is handled synchronously. The proposed closed-loop controller is shown to be semi-asymptotically stable by applying Lyapunov stability theory, and the effectiveness of the proposed methodology is demonstrated via numeric simulations of a homogeneous USV swarm.

1. Introduction

In recent decades, motion control problems for unmanned systems have received considerable attention from control communities. Research into unmanned surface vehicles (USVs) is a major research topic in this field. USV research topics have focused on path planning, path following and maintaining formation. [1–4]. Two significant trends have recently become noticeable in USV motion control studies. One trend is to imbue the control system with intelligence, with the goal of achieving autonomous control of USVs. The other trend is to extend autonomous control from single vessels to multiple vessels.

So far, studies involving multiple vessels have mainly focused on maintaining formation, obstacle avoidance and maintaining connectivity [5–7]. Extensive studies have been conducted with regard to maintaining formation; the studied objects have included satellites, aircraft, vessels and underwater vehicles. As this area of research has progressed, three dominant methods of formation control have been universally acknowledged: the leader-follower method [6–8], the virtual structure method [9,10] and the behavior-based method [11]. While outwardly different, these three approaches are essentially similar; they treat a formation as a rigid structure and force each member to achieve and maintain a designated relative position. In formation control studies, other methods such as the graph theory-based method [12], the artificial potential field (APF) method [13,14] and the fast marching method [15,16] have been applied to tackle obstacle avoidance problems and preserving connectivity while maintaining a desired formation. The issue of connectivity control for a multi-mechanism system was studied in Dimarogonas [17] and Sabattini [18], who developed the APF method to construct virtual force models. Liu and Bucknall [19] proposed a novel path-planning algorithm for USV formation based on the fast marching method. In addition, its use of APF when operating in dynamic environments was encouraging.

Formation control methods can preserve desired formation shapes well, and theories concerning these methods have matured. However, two problems have not yet been completely solved. First, the formation's shape is usually fixed in these formation control approaches; thus, the control systems may fail in situations that involve external obstacle avoidance [20]. Second, formation flexibility is limited because of the predefined formation shapes; thus, the individuals in the formation lack autonomy to make self-decisions.

In order to overcome the above problems and achieve more in-depth research on multi-mechanism cooperation, researchers have found inspiration in swarm intelligence ideas that are now widely used in studies of optimization algorithms [21–24]. Recently, the concept of swarm control was proposed [25–27]. Swarm intelligence is a characteristic of natural swarms such as bees and ant colonies, and the concept has inspired some successful

* Corresponding author.
E-mail address: drlinzhuang@163.com (Z. Lin).

http://dx.doi.org/10.1016/j.apor.2017.04.013
0141-1187/

approaches—including particle swarm optimization and ant colony optimization. Swarm control methods share some similarity with swarm optimization algorithms because both use a collection of individuals and can be regarded as an intelligent formation control method in which each individual is controlled separately rather than treating the entire formation as a fixed structure. If each individual in the swarm is self-organized while performing the collective tasks, autonomous group control can be achieved [28,29].

As for the specific implementation of a swarm control method, two primary issues should be studied first: swarm robotic flocking and autonomous collision avoidance. The most common method of modeling swarm flocking is with the Boids model. Cepeda-Gomez et al. [28] proposed a robust sliding mode control strategy and implemented it on two competing swarms, termed pursuers and evaders. Liu [30] studied the problem of bilateral human-swarm interaction, which enables a human operator to monitor and interact with a robot swarm in a remote area. This study proposed a task-oriented control framework for robots with two degrees of freedom (DOF). For the latter one, the APF method is often employed to introduce virtual forces between swarm members and obstacles [31,32]. Etemadi et al.[33] studied swarm motion in static environments and proposed an interactive effect model of attractive and repulsive forces to maintain the desired spacing between members. It is important to note that the swarm control studies to date have focused primarily on mobile robots; USV swarms have not yet been fully researched.

Motived by the studies described above, this paper investigates the problem of autonomous control for an underactuated USV swarm by exploiting a hierarchical control framework associated with specific algorithms. For the goal of autonomous group navigation for USVs, this study addresses the problem from four aspects: flocking strategy design, collision avoidance design, motion planning for each individual and control input design for underactuated USVs. The flocking strategy is inspired by Liu [30] and Franchi [34] and uses average position and distance variance instead of designating the position of each individual. For the purpose of implementing automatic obstacle avoidance and avoid collisions between swarm members, the APF method is adopted to design virtual repulsive forces. Moreover, the APF method has been improved from two aspects: adding a damping coefficient in potential functions and discretizing the outline of obstacles. Because the USVs are underactuated, the APF method cannot be used directly to control the USV swarm. Thus, we conduct real-time motion planning for the orientation and resultant velocity of each USV to account for the underactuated USVs. Then, in the last part, the sliding mode method is used to achieve robust control of the USVs. Finally, an integrated control system for USV swarm is formed by combining these approaches.

This paper is organized as follows. A dynamic model for the USV swarm is introduced in Section 2. Section 3 describes the design of the hierarchical control system for a USV swarm and addresses target tracking, obstacle avoidance and collision avoidance tasks. In addition, this section provides theoretical proof of the proposed algorithms. Section 4 presents numerical simulations showing the target tracking and obstacle avoidance capabilities of a USV swarm under the proposed control system.

2. Ship dynamics

Ship navigation on the sea occurs in six DOF, namely, surge, sway, heave, roll, pitch and yaw. But motion control for surface vehicles considers only 3 DOF in the horizontal plane, surge, sway and yaw. Pitch, roll and heave are ignored by convention. In this study, the controlled object is an underactuated USV swarm comprised of n USVs, in which each USV is equipped with one propeller and one rudder. The motion equations of the ith USV in the horizontal plane can be formulated as follows [35,36]:

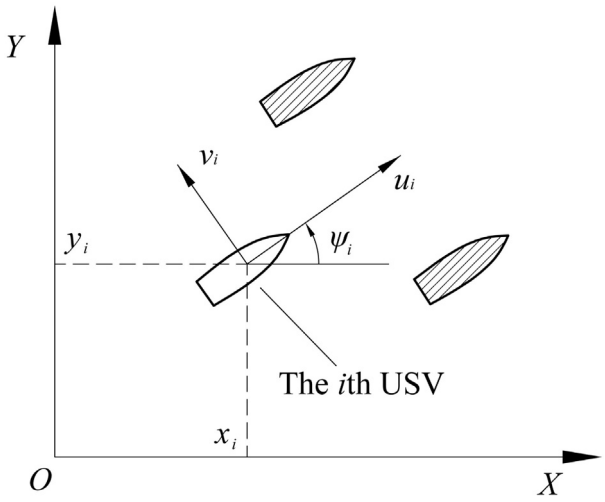

Fig. 1. Frame transformation in a horizontal plane.

$$\begin{cases} \dot{x}_i = u_i \cos\psi_i - v_i \sin\psi_i \\ \dot{y}_i = u_i \sin\psi_i + v_i \cos\psi_i \\ \dot{\psi}_i = r_i \\ \dot{u}_i = \dfrac{m_{22}}{m_{11}} v_i r_i - \dfrac{d_u}{m_{11}} u_i - \dfrac{d_{|u|u}}{m_{11}} |u_i| u_i + \dfrac{1}{m_{11}} \tau_{ui} + \xi_{ui}, \\ \dot{v}_i = -\dfrac{m_{11}}{m_{22}} u_i r_i - \dfrac{d_v}{m_{22}} v_i - \dfrac{d_{|v|v}}{m_{22}} |v_i| v_i + \xi_{vi}, \\ \dot{r}_i = \dfrac{m_{11} - m_{22}}{m_{33}} u_i v_i - \dfrac{d_r}{m_{33}} r_i - \dfrac{d_{|r|r}}{m_{33}} |r_i| r_i + \dfrac{1}{m_{33}} \tau_{ri} + \xi_{ri}, \end{cases} \tag{1}$$

where x_i, y_i and ψ_i denote the position and orientation of the ith USV in the earth-fixed frame, respectively, u_i, v_i represent surge and sway velocities in the body-fixed frame, respectively, and r_i is the yaw rate. Here, m_{11}, m_{22}, m_{33} are inertial masses including hydrodynamic added mass, and $d_u, d_{|u|u}, d_v, d_{|v|v}, d_r, d_{|r|r}$ denote the hydrodynamic damping in surge, sway and yaw, respectively. τ_{ui}, τ_{ri} denote the surge force and yaw moment in the body-fixed frame, and ξ_{ui}, ξ_{vi}, and ξ_{ri} are external disturbances acting on the ship's hull caused by winds, waves and currents. A frame transformation of the ith USV is represented in Fig. 1.

Assumption 1. The inertial and damping coefficients in Eq. (1) are all positive constant, i.e. $m_{ii} > 0$, $d_{ii} > 0$. External disturbances are bounded, which satisfies the conditions of $|\xi_{ui}| \le \xi_{u\max}$, $|\xi_{vi}| \le \xi_{v\max}$, and $|\xi_{ri}| \le \xi_{r\max}$. Here, $\xi_{u\max}$, $\xi_{v\max}$, $\xi_{r\max}$ are constants.

Remark 1. For the sake of clarifying and simplifying the process of writing formulas and proofs, the USV swarm is assumed to be homogeneous; thus, the model parameters for each USV are the same. However, the control algorithm proposed later in this work is also suitable for controlling a heterogeneous swarm.

3. Motion controller design for USV swarm

This section describes the design of a hierarchical controller for a USV swarm based on control flow. Three task layers, flocking strategy design, motion planning and control input design, are defined to implement integrated swarm control. Fig. 2 shows the framework of the proposed closed-loop controller. The symbols used in the figure are explained later in the text. As depicted in the instruction delivery process shown in Fig. 2, the first layer of the swarm

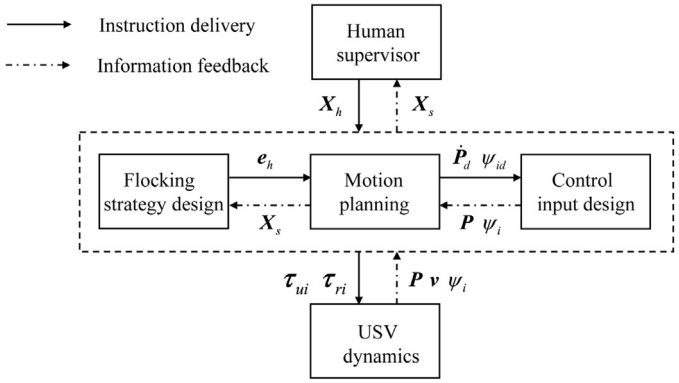

Fig. 2. Framework of the closed-loop controller.

controller implements a flocking strategy. In this layer, the flocking strategy is designed based on the swarm members' average positions and distance variances. The second layer is the motion planning layer, which plans the resultant velocity and yaw angle of each USV. The goal of this layer is to accomplish some tasks autonomously when the swarm is moving toward a target. The autonomous tasks include obstacle avoidance and avoiding collisions with other group members and are realized by including virtual repulsion potential functions. The last layer is the control input design, in which the surge thrust τ_{ui} and yaw moment τ_{ri} are designed by applying the sliding-mode method. This layer considers the underactuated characteristic of the USVs.

3.1. Flocking strategy design

In USV swarm control, a human supervisor rather than an operator is required to supervise the swarm. The supervisor does not need to control each USV continuously or design a special formation shape for the swarm; the supervisor needs only to formulate some basic orders. These orders will be transmitted to each USV through a wireless network. Subsequently, the USVs operate independently to fulfill those basic orders. The basic orders are primarily concerned with the mission objectives and swarm operating statuses, for example, the desired targets or waypoints or the spacing between group members.

A flocking strategy involves the way that swarm members gather and judge whether their relative positions are appropriate. Unlike formation control methods, the flocking strategy in this work is designed by defining a central location and controlling the variance of the distance between each USV and that central location. In order to express the flocking strategy mathematically, the position function of the swarm is designed as follows:

$$\boldsymbol{X_s} = [\bar{x}, \bar{y}, \sigma]^{\mathrm{T}}, \tag{2}$$

where

$$\bar{x} = \frac{1}{n}\sum_{i=1}^{n} x_i$$
$$\bar{y} = \frac{1}{n}\sum_{i=1}^{n} y_i$$
$$\sigma = \frac{1}{n^2}\sum_{i=1}^{n}[(x_i - \bar{x})^2 + (y_i - \bar{y})^2].$$

Here, $(\bar{x}, \bar{y})$ denotes the center position of the swarm in the earth-fixed frame, and σ denotes the distance variance of the swarm members.

Then, the desired position function, $\boldsymbol{X}_h$, and the error variable of the desired position function, $\boldsymbol{e}_h$, are further designed as follows:

$$\begin{cases} \boldsymbol{X}_h = [\bar{x}_d, \bar{y}_d, \sigma_d]^T \\ \boldsymbol{e}_h = \boldsymbol{X_s} - \boldsymbol{X}_h = [e_1, e_2, e_3]^T \end{cases} \tag{3}$$

where $\bar{x}_d, \bar{y}_d$ and $\bar{\sigma}_d$ denote the desired values of $\bar{x}, \bar{y}$ and σ, respectively. e_1, e_2, and e_3 are components of $\boldsymbol{e}_h$. If the swam members reach the target point and maintain the desired distance between each other, then $\boldsymbol{e}_h$ will converge to zero.

Remark 2. Two symbol definitions, i.e. $\dot{A}$ and $\frac{\partial A}{\partial B}$, will be largely used later in the formula derivation; $\dot{A}$ denotes the time derivative of variable A, and $\frac{\partial A}{\partial B}$ denotes the partial derivative of A with respect to B. It should be noted that both A and B can be either a scalar or a matrix.

We define the position vector of each USV as $\boldsymbol{P}_i = (x_i, y_i)^T$ and the position vector of the swarm as $\boldsymbol{P} = (\boldsymbol{P}_1^T, \boldsymbol{P}_2^T, \ldots, \boldsymbol{P}_n^T)^T$, $\boldsymbol{P} \in R^{2n\times 1}$. Then, differentiating Eq. (2) yields:

$$\dot{\boldsymbol{X}}_{\boldsymbol{s}} = \boldsymbol{J_s}(\boldsymbol{P})\dot{\boldsymbol{P}}, \tag{4}$$

where $\dot{\boldsymbol{P}} \in R^{2n\times 1}$ denotes the velocity vector in the earth-fixed frame, and $\boldsymbol{J_s}(\boldsymbol{P})$ is a Jacobian matrix with the following form:

$$\begin{aligned} \boldsymbol{J_s}(\boldsymbol{P}) &= \frac{\partial \boldsymbol{X}_s}{\partial \boldsymbol{P}} = \left[\frac{\partial \bar{x}}{\partial \boldsymbol{P}}^T, \frac{\partial \bar{y}}{\partial \boldsymbol{P}}^T, \frac{\partial \sigma}{\partial \boldsymbol{P}}^T\right]^T \in R^{3\times 2n} \\ \frac{\partial \bar{x}}{\partial \boldsymbol{P}} &= \frac{1}{n}(1, 0, 1, 0, \ldots, 1, 0)^T, \quad \frac{\partial \bar{x}}{\partial \boldsymbol{P}} \in R^{2n\times 1} \\ \frac{\partial \bar{y}}{\partial \boldsymbol{P}} &= \frac{1}{n}(0, 1, 0, 1, \ldots, 0, 1)^T, \quad \frac{\partial \bar{y}}{\partial \boldsymbol{P}} \in R^{2n\times 1} \\ \frac{\partial \sigma}{\partial \boldsymbol{P}} &= \frac{2(n-1)}{n^3}(\ldots, x_i - \bar{x}, y_i - \bar{y}, \ldots)^T, \quad \frac{\partial \sigma}{\partial \boldsymbol{P}} \in R^{2n\times 1}. \end{aligned} \tag{5}$$

We define $\boldsymbol{J_s^+}(\boldsymbol{P}) \in R^{2n\times 3}$ as the pseudo-inverse matrix of $\boldsymbol{J_s}(\boldsymbol{P})$, and it has the following properties (explained in Ref. [37]):

$$\begin{aligned} \boldsymbol{J_s^+} &= \boldsymbol{J_s}^T(\boldsymbol{J_s}\boldsymbol{J_s}^T)^{-1} \\ \boldsymbol{J_s}\boldsymbol{J_s}^+ &= \boldsymbol{I}_3, \end{aligned} \tag{6}$$

where $\boldsymbol{I}_3$ is a 3rd-order identity matrix.

3.2. Motion planning for each USV

After designing the flocking strategy, the next step in the control flow is to perform motion planning for each USV. Motion planning in this paper is not performed to plan the desired path but to plan a desired orientation and desired resultant velocity for each USV in real time. During motion planning, two primary issues must considered simultaneously: one is to make $\boldsymbol{e}_h$ converge to $\boldsymbol{0}$ and the other is to avoid collisions between the swarm members and external obstacles. Before motion planning, the APF method is adopted and improved to implement obstacle avoidance and collision avoidance for each USV during target tracking. More specifically, the artificial potential functions for obstacle avoidance and avoiding collisions between swarm members will be designed next in this section. In addition, the APF method is enhanced by adding a damping coefficient and discretizing the outline of obstacles, which improves the applicability of the proposed method. Then, using the Lyapunov method and taking both $\boldsymbol{e}_h$ and the potential functions into consideration, we obtain the desired velocity and orientation for each USV.

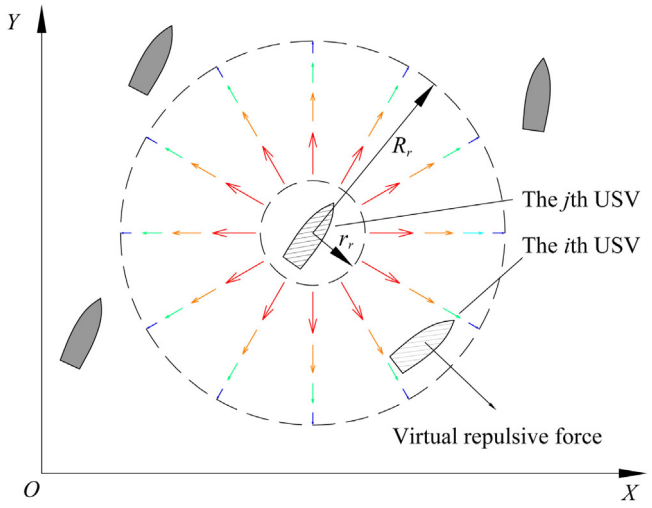

Fig. 3. Schematic of the virtual potential field around the jth USV.

3.2.1. Potential function design for avoiding collision between swarm members

Collisions between swarm members can be avoided by setting up a restricted perimeter around each USV. This restricted perimeter can be round; its radius is termed the "minimum safe distance". In Ref. [30,38], a local potential field is used to avoid collisions between the members of a 2-DOF robot swarm. The idea behind a virtual potential function is adopted by this paper, and the potential function for collision avoidance is shown below:

$$\Phi_{rj} = \sum_{i=1}^{n} \Phi_{rji} = \sum_{i=1}^{n} \left\{ \min\left(0, \frac{d(i,j)^2 - R_r^2}{d(i,j)^2 - r_r^2}\right)\right\}^2, \quad j = 1, 2, \ldots, n, \tag{7}$$

where $d(i,j) = [(x_i - x_j)^2 + (y_i - y_j)^2]^{1/2}$ is the distance between the ith and jth USVs, and R_r and r_r denote the maximum and minimum safe distances, respectively.

The essence of Eq. (7) is to build a ring-shaped potential field around the jth USV in the region of $r_r < d(i,j) < R_r$ and to impose a repulsive force on the ith USV in the radial direction. Fig. 3 presents a schematic of the virtual potential field around the jth USV to make Eq. (7) more comprehensible. After the control parameters have been confirmed, the direction and magnitude of the virtual repulsive forces relate only to the relative positions of neighboring USVs.

Differentiating Eq. (7) along $\boldsymbol{P}$, we obtain:

$$\frac{\partial \Phi_{rj}}{\partial \boldsymbol{P}} = \sum_{i=1}^{n} \frac{\partial \Phi_{rji}}{\partial \boldsymbol{P}} = \left[\ldots, \left(\frac{\partial \Phi_{rji}}{\partial \boldsymbol{P}_i}\right)^T, \ldots\right]^T \in R^{2n\times 1}, \tag{8}$$

where

$$\frac{\partial \Phi_{rji}}{\partial \boldsymbol{P}_i} = \begin{cases} 4\dfrac{(R_r^2 - r_r^2)(d(i,j)^2 - R_r^2)}{(d(i,j)^2 - r_r^2)^3}(\boldsymbol{P}_i - \boldsymbol{P}_j), & \text{if } r_r < d(i,j) < R_r \\ 0, & \text{if } d(i,j) > R_r \text{ or } d(i,j) < r_r. \end{cases}$$

Remark 3. $\frac{\partial \Phi_{rji}}{\partial \boldsymbol{P}_i}$ denotes the virtual repulsive force imposed on the ith USV. As designed in Eq. (7), the potential function, Φ_{rji}, is set to be zero when $d(i,j) \geq R_r$ or $d(i,j) \leq r_r$; and it increases rapidly when $d(i,j)$ decreases, if $r_r \leq d(i,j) < R_r$. The physical effects of this function are easy to explain: $d(i,j) \geq R_r$ means that the two USVs will maintain a safe distance; thus, repulsive force is not required. The $d(i,j) < r_r$ denotes the ith USV sailing into the restricted perimeter, which is not allowed; it is only in the area of $r_r \leq d(i,j) < R_r$ that $\Phi_{rji} \neq 0$ and the potential function applies, and $\Phi_{rj} = \infty$ if $d(i,j) = r_r$. Thus, this avoids the situation where $d(i,j) < r_r$, given the initial precondition that $d(i,j) > r_r$.

3.2.2. Potential function design for obstacle avoidance

During USV navigation, obstacles may occur along the course such as reefs or islets. Thus, automatic obstacle avoidance is another major problem that needs to be solved for the purpose of autonomous navigation. Similar to collision avoidance, the potential function method is also suitable for use in obstacle avoidance and can be designed similarly to Eq. (7). For example, assume the position of each obstacle is known, there are m obstacles, and the position of the jth obstacle is defined as $o_j = (o_{xj}, o_{yj})$, for $j = 1, 2, \cdots, m$. Then, the potential function of obstacle avoidance can be preliminarily designed as follows:

$$\Phi_{oj} = \sum_{i=1}^{n} \left\{ \min\left(0, \frac{d(i,o_j)^2 - R_o^2}{d(i,o_j)^2 - r_o^2}\right)\right\}^2, \quad j = 1, 2, \ldots, m, \tag{9}$$

where $d(i,o_j) = [(x_i - ox_j)^2 + (y_i - oy_j)^2]^{1/2}$ is the distance between the ith USV and the jth obstacle and R_o and r_o denote the maximum and minimum safe distances for obstacle avoidance, respectively.

Just as in Eq. (7), the essence idea of Eq. (9) is to construct a ring-shaped potential field around each obstacle in the region of $r_o < d(i,o_j) < R_o$. However, this function has the underlying disadvantage, that USVs may not bypass such obstacles smoothly. The paths of USVs sailing by such an obstacle will bounce like a spring, causing them to deviate too far away from their original course. To overcome this problem, Eq. (9) can be improved by adding a velocity damping coefficient $k(\dot{d}(i,o_j))$, as shown in following equation:

$$\Phi_{oj} = \sum_{i=1}^{n} [0.5 + k(\dot{d}(i,o_j))] \left\{ \min\left(0, \frac{d(i,o_j)^2 - R_o^2}{d(i,o_j)^2 - r_o^2}\right)\right\}^2, \quad j = 1, 2, \ldots, m, \tag{10}$$

where

$$k(\dot{d}(i,o_j)) = \begin{cases} \arctan(-\dot{d}(i,o_j)), & \text{if } \dot{d}(i,o_j) < 0 \\ 0, & \text{if } \dot{d}(i,o_j) \geq 0, \end{cases} \tag{11}$$

and $\dot{d}(i,o_j)$ denotes the relative velocity between USV i and obstacle j. Thus, the damping coefficient $k(\dot{d}(i,o_j))$ is negatively correlated with $\dot{d}(i,o_j)$ when $\dot{d}(i,o_j) < 0$, and it equals zero when $\dot{d}(i,o_j) \geq 0$.

Either Eq. (9) or (10) can be used to avoid round-shaped obstacles. However, obstacles cannot always be replaced by circles in practice, which limit the use of these potential functions. To implement obstacle avoidance for arbitrary shapes, this study adopts the approach of discretizing the obstacles outlines instead.

First, the outline of the jth obstacle is discretized into l points, and the coordinates of each point are defined as $\boldsymbol{O}_{jk} = (ox_{jk}, oy_{jk})^T$, for $k = 1, 2, \ldots, l$. Then, the distance of the USVs to the discretized points is defined as $d(i,o_{jk}) = [(x_i - ox_{jk})^2 + (y_i - oy_{jk})^2]^{1/2}$, for $i = 1, 2, \ldots, n$ and $k = 1, 2, \ldots, l$. Implementing obstacle avoidance then requires only that the USVs maintain a safe distance from the obstacle outlines; in other words, they simply need to satisfy the condition $d(i,o_{jk}) > r_o$. Then, obstacle distance is redefined as follows:

$$d(i,o_j) = \min[\ldots, d(i,o_{jk}), \ldots], \quad k = 1, 2, \ldots, l. \tag{12}$$

If we combine Eq. (10) and (12), the artificial potential field can be adjusted to the irregular boundary by auto-changing the interaction point according to the ith USV's position. Thus, the virtual repulsive force imposed on each USV is related to the obstacle's shape, the USV's velocity and the relative positions of obstacles and USVs.

Take the partial derivative of Eq. (10) concerning $\boldsymbol{P}$:

$$\frac{\partial \Phi_{oj}}{\partial \boldsymbol{P}} = \sum_{i=1}^{n} \frac{\partial \Phi_{oji}}{\partial \boldsymbol{P}} = \left[\ldots, \left(\frac{\partial \Phi_{oji}}{\partial \boldsymbol{P}_i} \right)^T, \ldots \right]^T \in R^{2n\times 1}, \tag{13}$$

where

$$\frac{\partial \Phi_{oji}}{\partial \boldsymbol{P}_i} = \begin{cases} 4\dfrac{(R_o^2 - r_o^2)(d(i,o_j)^2 - R_o^2)}{(d(i,o_j)^2 - r_o^2)^3}(\boldsymbol{P}_i - \boldsymbol{O}_j), & \text{if } r_o < d(i,o_j) < R_o \\ 0, & \text{if } d(i,o_j) > R_o \text{ or } d(i,o_j) < r_o, \end{cases}$$

and $\boldsymbol{O}_j$ denotes the position of the boundary point that is closest to the ith USV.

3.2.3. Planning of desired orientation and resultant velocity

With the design of the potential functions complete, we now design the desired orientation ψ_{id} and resultant velocity V_{id} for each USV. In motion planning, tasks such as USV flocking, obstacle avoidance and avoiding collisions between swarm members should be considered jointly. The judgment criterion these tasks fulfill is to converge the values of $\boldsymbol{e}_h$, Φ_{oj} and Φ_{rj} to $\boldsymbol{0}$ or 0, respectively.

Because all the potential functions are non-negative scalars, they can be summed. Thus, the total potential function is designed as follows:

$$\Phi = k_1 \sum_{j=1}^{m} \Phi_{oj} + k_2 \sum_{j=1}^{n} \Phi_{rj} \geq 0, \tag{14}$$

where k_1 and k_2 are weight coefficients whose values must be properly selected.

Then, we define the Lyapunov function candidate V_1 as follows:

$$V_1 = \frac{1}{2}\boldsymbol{e}_h^T \boldsymbol{K}_1 \boldsymbol{e}_h + k_3 \Phi, \tag{15}$$

where $\boldsymbol{K}_1 = diag(k_{11}, k_{22}, k_{33})$ denotes the weight matrix to each variable of $\boldsymbol{e}_h$, and k_3 is the weight coefficient of the potential function.

Differentiating both sides of Eq. (15) yields:

$$\begin{aligned} \dot{V}_1 &= \boldsymbol{e}_h^T \boldsymbol{K}_1 \dot{\boldsymbol{e}}_h + k_3 \boldsymbol{\varphi}^T \dot{\boldsymbol{P}} = \boldsymbol{e}_h^T \boldsymbol{K}_1 (\boldsymbol{J}_s \dot{\boldsymbol{P}} - \dot{\boldsymbol{X}}_h) + k_3 \boldsymbol{\varphi}^T \dot{\boldsymbol{P}} \\ &= (\boldsymbol{e}_h^T \boldsymbol{K}_1 \boldsymbol{J}_s + k_3 \boldsymbol{\varphi}^T)\dot{\boldsymbol{P}} - \boldsymbol{e}_h^T \boldsymbol{K}_1 \dot{\boldsymbol{X}}_h, \end{aligned} \tag{16}$$

where $\boldsymbol{\varphi}$ is a simplified replacement of $(\frac{\partial \Phi}{\partial \boldsymbol{P}})^T$ for notational convenience. Then, we design the desired swarm velocity vector $\dot{\boldsymbol{P}}_d$ as follows:

$$\dot{\boldsymbol{P}}_d = (\dot{\boldsymbol{P}}_{1d}^T, \dot{\boldsymbol{P}}_{2d}^T, \ldots, \dot{\boldsymbol{P}}_{nd}^T)^T = -(\boldsymbol{J}_s^T \boldsymbol{K}_1 \boldsymbol{e}_h + k_3 \boldsymbol{\varphi}) + \boldsymbol{J}_s^+ \dot{\boldsymbol{X}}_h, \tag{17}$$

where $\dot{\boldsymbol{P}}_{id} = (\dot{x}_{id}, \dot{y}_{id})^T$ is the desired velocity vector of the ith USV in the earth-fixed frame.

Then, the error variable of the swarm velocity vector is defined as follows:

$$\tilde{\boldsymbol{P}} = \dot{\boldsymbol{P}} - \dot{\boldsymbol{P}}_d = (\tilde{\boldsymbol{P}}_1^T, \tilde{\boldsymbol{P}}_2^T, \ldots, \tilde{\boldsymbol{P}}_n^T)^T, \tag{18}$$

where $\tilde{\boldsymbol{P}}_i = \dot{\boldsymbol{P}}_i - \dot{\boldsymbol{P}}_{id}$ denotes the velocity vector error of the ith USV, for $i = 1, 2, \ldots, n$.

Substituting Eq. (16) into Eq. (15) yields

$$\begin{aligned} \dot{V}_1 = &-(\boldsymbol{J}_s^T \boldsymbol{K}_1 \boldsymbol{e}_h + k_3 \boldsymbol{\varphi})^T (\boldsymbol{J}_s^T \boldsymbol{K}_1 \boldsymbol{e}_h + k_3 \boldsymbol{\varphi}) \\ &+ (\boldsymbol{J}_s^T \boldsymbol{K}_1 \boldsymbol{e}_h + k_3 \boldsymbol{\varphi})^T \tilde{\boldsymbol{P}} - \boldsymbol{\varphi}^T \boldsymbol{J}_s^+ \dot{\boldsymbol{X}}_h. \end{aligned} \tag{19}$$

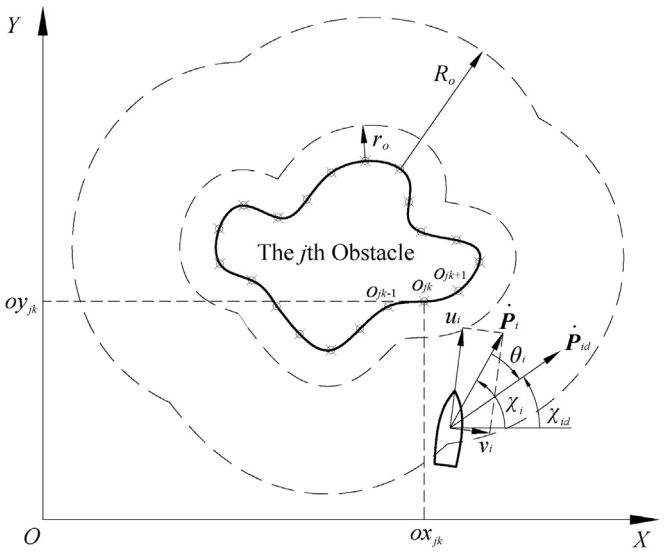

Fig. 4. Schematic of obstacle discretization and orientation planning.

For each USV, the resultant velocity is defined as $V_i = \sqrt{\dot{\boldsymbol{P}}_i^T \dot{\boldsymbol{P}}_i} = \sqrt{u_i^2 + v_i^2}$. In order to make $\tilde{\boldsymbol{P}}_i$ convergent, the desired resultant velocity and desired velocity angle of each USV is defined as follows:

$$\begin{cases} V_{id} = \sqrt{\dot{\boldsymbol{P}}_{id}^T \dot{\boldsymbol{P}}_{id}} = \sqrt{\dot{x}_{id}^2 + \dot{y}_{id}^2}, \\ \chi_{id} = \arctan 2(\dot{y}_{id}, \dot{x}_{id}), \end{cases} \quad i = 1, 2, \ldots, n. \tag{20}$$

The angle error of the resultant velocity is defined as: $\theta_i = \chi_i - \chi_{id}$, and $\chi_{id} = \psi_{id} + \arctan\left(\frac{v_i}{u_i}\right)$. Thus, the resultant velocity angle error can be called desired yaw angle error and further modified as follows:

$$\theta_i = \chi_i - \chi_{id} = \psi_i - \psi_{id}. \tag{21}$$

Now, the motion planning of the swarm is finished. Fig. 4 shows the orientation planning and obstacle discretization processes.

The subsequent design process will use the variables $\dot{\psi}_{id}$ and $\ddot{\psi}_{id}$, but to avoid numerical differentiation of ψ_{id}, the following second-order filter is introduced:

$$\ddot{\psi}_i^{\alpha} + 2\zeta\omega\dot{\psi}_i^{\alpha} + \omega^2(\psi_i^{\alpha} - \psi_{id}) = 0, \tag{22}$$

where $\ddot{\psi}_i^{\alpha}$, $\dot{\psi}_i^{\alpha}$ and ψ_i^{α} are the estimate values corresponding to $\ddot{\psi}_{id}$, $\dot{\psi}_{id}$ and ψ_{id}, respectively. Later, in the formulas, $\ddot{\psi}_{id}$ and $\dot{\psi}_{id}$ will be replaced by $\ddot{\psi}_i^{\alpha}$ and $\dot{\psi}_i^{\alpha}$.

We define the Lyapunov function candidate, V_2, as follows:

$$V_2 = \frac{1}{2}\tilde{\boldsymbol{P}}^T \tilde{\boldsymbol{P}} = \frac{1}{2}\sum_{i=1}^{n} \tilde{\boldsymbol{P}}_i^T \tilde{\boldsymbol{P}}_i. \tag{23}$$

Then, Eq. (23) can be transformed as follows:

$$\begin{aligned} V_2 &= \frac{1}{2}\sum_{i=1}^{n} \tilde{\boldsymbol{P}}_i^T \boldsymbol{R}(\chi_i)^T \boldsymbol{R}(\chi_i) \tilde{\boldsymbol{P}}_i \\ &= \frac{1}{2}\sum_{i=1}^{n} [(V_i - V_{id}\cos\theta_i)^2 + V_{id}^2 \sin^2\theta_i] \\ &= \frac{1}{2}\sum_{i=1}^{n} [(V_i - V_{id})^2 + 4V_i V_{id} \sin^2(\theta_i/2)] \\ &\leq \frac{1}{2}\sum_{i=1}^{n} [(V_i - V_{id})^2 + \lambda\theta_i^2], \end{aligned} \tag{24}$$

where

$$\boldsymbol{R}(\chi_i) = \begin{bmatrix} \cos\chi_i & -\sin\chi_i \\ \sin\chi_i & \cos\chi_i \end{bmatrix},$$

and $\boldsymbol{R}(\chi_i)$ is the rotation matrix, which has the property that $\boldsymbol{R}(\chi_i)^{-1} = \boldsymbol{R}(\chi_i)^T$. Here, λ is a positive constant, and we assume it meets the condition $\lambda \geq V_i V_{id}$.

3.3. Control input design

The last step of the control flow is to design the control inputs, while considering the underactuated characteristic of USVs. Numerous studies have addressed underactuated ships, in which the most common approach is to design the surge force τ_{ui} and yaw moment τ_{ri} separately according to the desired resultant velocity and orientation. In controller design, the backstepping approach and the sliding-mode method are often used. Compared to the backstepping approach, the sliding-mode method is more robust to parametric uncertainty and external disturbances. Thus, the sliding-mode method is applied here to design the control inputs τ_{ui} and τ_{ri}. The yaw moment τ_{ri} must be properly designed before tackling τ_{ui}. Consequently, a first-order sliding manifold about θ_i is designed as follows:

$$S_1 = \dot{\theta}_i + \lambda_1 \theta_i = 0 \tag{25}$$

Then, the Lyapunov function candidate V_3 is designed as shown below:

$$V_3 = \frac{1}{2} S_1^2. \tag{26}$$

Differentiating both sides of Eq. (26) yields

$$\begin{aligned} \dot{V}_3 &= S_1 \dot{S}_1 = S_1(\ddot{\theta}_i + \lambda_1 \dot{\theta}_i) \\ &= S_1[\dot{r}_i - \ddot{\psi}_i^{\alpha} + \lambda_1(r_i - \dot{\psi}_i^{\alpha})], \end{aligned} \tag{27}$$

and substituting Eq. (1) into Eq. (27) yields

$$\begin{aligned} \dot{V}_3 = S_1 \Big[&\frac{m_{11} - m_{22}}{m_{33}} u_i v_i - \frac{1}{m_{33}}(d_r + d_{|r|r}|r_i|)r_i + \frac{1}{m_{33}}\tau_{ri} \\ &+ \xi_{ri} - \ddot{\psi}_i^{\alpha} + \lambda_1(r - \dot{\psi}_i^{\alpha}) \Big]. \end{aligned} \tag{28}$$

The yaw moment τ_{ri} is then designed as follows:

$$\begin{aligned} \tau_{ri} = m_{33}[&\ddot{\psi}_i^{\alpha} + \lambda_1(\dot{\psi}_i^{\alpha} - r) - \frac{m_{11} - m_{22}}{m_{33}} u_i v_i \\ &+ \frac{d_r}{m_{33}} r_i + \frac{d_{|r|r}}{m_{33}} |r_i| r_i + \tau], \end{aligned} \tag{29}$$

where τ is a control variable that still requires further design.

Substituting Eq. (29) into Eq. (28) yields

$$\begin{aligned} \dot{V}_3 &= S_1[\tau + \xi_r] \\ &\leq |S_1|[\tau\, \mathrm{sgn}(S_1) + \xi_{\max}]. \end{aligned} \tag{30}$$

We can design τ as follows:

$$\tau = -(k_4 + \xi_{r\,\max})\mathrm{sgn}(S_1), \tag{31}$$

where $\mathrm{sgn}(S_1)$ is the switching function, which has the following form:

$$sgn(S_1) = \begin{cases} 1, & S_1 > 0 \\ 0, & S_1 = 0 \\ -1, & S_1 < 0 \end{cases}.$$

Then, Eq. (28) can be transformed into

$$\dot{V}_3 \leq -k_4 |S_1|. \tag{32}$$

Hence, the sliding manifold is asymptotically stable and it will reach the manifold of $S_1 = 0$ in finite time and then maintain that state. Thus it can make θ_i asymptotically stable, i.e. $(\dot{\theta}_i, \theta_i) \to (0, 0)$.

However, there is a conspicuous discontinuity in the switching function $\mathrm{sgn}(S_1)$ that will make the feedback control law discontinuous. Other studies on the sliding-mode control such as [39,40] have explained the chattering effect in detail. In this type of feedback control, a chattering effect near the zero point may occur in the control input, which introduces high-frequency dynamics into the system's response, which will eventually affect the performance and robustness of the controller. For avoiding this potential chattering effect, an alternative method is to use a continuous switch function to replace $\mathrm{sgn}(S_1)$. Therefore, the saturation function $\mathrm{sat}(S_1)$ is adopted, which is defined as follows:

$$\mathrm{sat}(S_1) = \begin{cases} S_1/\kappa, & |S_1| \leq \kappa \\ \mathrm{sgn}(S_1), & |S_1| > \kappa, \end{cases} \tag{33}$$

where $\kappa > 0$ is the boundary layer thickness.

After substituting $\mathrm{sat}(S_1)$ and Eq. (31) into Eq. (29), we obtain the final form of the yaw moment:

$$\begin{aligned} \tau_{ri} = m_{33} \Big[&\ddot{\psi}_i^{\alpha} + \lambda_1(\dot{\psi}_i^{\alpha} - r) - \frac{m_{11} - m_{22}}{m_{33}} u_i v_i \\ &+ \frac{d_r}{m_{33}} r_i + \frac{d_{|r|r}}{m_{33}} |r_i| r_i - (k_4 + \xi_{r\,\max})\mathrm{sat}(S_1) \Big]. \end{aligned} \tag{34}$$

Then, Eq. (30) can be recomposed as follows:

$$\begin{aligned} \dot{V}_3 &\leq S_1[\tau + \xi_{r\,\max}\mathrm{sgn}(S_1)] \\ &= -k_4 S_1 \mathrm{sat}(S_1) + S_1 \xi_{r\,\max}(\mathrm{sgn}(S_1) - \mathrm{sat}(S_1)). \end{aligned} \tag{35}$$

There are two situations that involve Eq. (35) with respect to the value of $|S_1|$. Each situation is addressed separately below.

Situation A: $|S_1| \geq \kappa$.

In this situation, $\mathrm{sat}(S_1) = \mathrm{sgn}(S_1)$; therefore, Eq. (35) transforms to

$$\dot{V}_3 \leq -k_4 S_1 \mathrm{sgn}(S_1) = -k_4 |S_1| \leq 0. \tag{36}$$

Situation B: $|S_1| < \kappa$.

In this situation, $\mathrm{sat}(S_1) = S_1/\kappa$; therefore, Eq. (35) transforms to

$$\begin{aligned} \dot{V}_3 &\leq -\frac{k_4}{\kappa} S_1^2 + \xi_{r\,\max}(1 - \frac{1}{\kappa}|S_1|)|S_1| \\ &\leq -\frac{k_4}{\kappa} S_1^2 + \frac{\kappa}{4}\xi_{r\,\max} \\ &= -\frac{2k_4}{\kappa} V_3 + \frac{\kappa}{4}\xi_{r\,\max}. \end{aligned} \tag{37}$$

Considering these two situations and referring to the convergence proof given in [41], the value of V_3 at any time can be bounded as follows:

$$0 \leq V_3(t) \leq V_3(0) e^{-\frac{2k_4}{\kappa}t} + \frac{\kappa^2 \xi_{r\,\max}}{8k_4}. \tag{38}$$

Under the effect of the control input τ_{ri}, the sliding manifold S_1 will converge to the region of $\{S_1 | |S_1| < \kappa\}$ in finite time and then maintain it. By magnifying k_4 and decreasing κ appropriately, the residual convergence error can be minimized to an acceptable range, and the same is true for θ_i.

After designing τ_{ri}, we need to design the surge force τ_{ui}. We first define the following Lyapunov function candidate V_4:

$$V_4 = \frac{1}{2}(V_i - V_{id})^2. \tag{39}$$

Differentiating both sides of Eq. (39) yields

$$\begin{aligned}\dot{V}_4 &= (V_i - V_{id})(\dot{V}_i - \dot{V}_{id}) \\ &= (V_i - V_{id})\left[\frac{1}{V}_i(u_i\dot{u}_i + v_i\dot{v}_i) - \dot{V}_{id}\right] \\ &= (V_i - V_{id})\left[\frac{u_i}{V_i}\left(\frac{m_{22}}{m_{11}}v_i r_i - \frac{1}{m_{11}}(d_u + d_{|u|u}|u_i|)u_i \right.\right. \\ &\quad \left.\left. + \frac{1}{m_{11}}\tau_{ui} + \xi_{ui}\right) + \frac{1}{V}_i v_i\dot{v}_i - \dot{V}_{id}\right].\end{aligned} \tag{40}$$

Then, we design the sliding manifold S_2 and surge force τ_{ui} as follows:

$$S_2 = V_i - V_{id} = 0 \tag{41}$$

$$\tau_{ui} = m_{11}\left[-\frac{m_{22}}{m_{11}}v_i r_i + \frac{1}{m_{11}}(d_u + d_{|u|u}\left|u_i\right|)u_i - k_5\mathrm{sat}(S_2)\right], \tag{42}$$

where k_5 is a positive constant.

Substituting Eq. (42) into Eq. (40) yields

$$\begin{aligned}\dot{V}_4 &= S_2\frac{u_i}{V_i}(\xi_{ui} - k_5\mathrm{sat}(S_2)) + S_2\left(\frac{1}{V}_i v_i\dot{v}_i - \dot{V}_{id}\right) \\ &\le -k_5\frac{u_i}{V_i}S_2\,\mathrm{sat}(S_2) + \varepsilon|S_2|,\end{aligned} \tag{43}$$

where

$$\varepsilon = \frac{1}{V}_i(|u_i|\xi_{u\,\max} + |v_i\dot{v}_i|) + |\dot{V}_{id}|. \tag{44}$$

Because the sway speed v_i is passively stabilized as explained in [42], and because u_i, V_i and $\xi_{u\max}$ are all bounded and ε is both bounded and positive. Then, Eq. (43) will be discussed for two cases similarly to Eq. (35).

Situation A: $|S_2| \ge \kappa$.

In this situation, $\mathrm{sat}(S_2) = \mathrm{sgn}(S_2)$; therefore, Eq. (43) transforms to

$$\dot{V}_4 \le -k_5\frac{u_i}{V_i}|S_2| + \varepsilon|S_2|. \tag{45}$$

If we properly choose k_5 so that it meets the condition $k_5 \ge \frac{\varepsilon V_i}{u_i}$, we obtain

$$\dot{V}_4 \le -\left(k_5\frac{u_i}{V_i} - \varepsilon\right)|S_2| \le 0. \tag{46}$$

Situation B: $|S_2| < \kappa$.

In this situation, $\mathrm{sat}(S_2) = S_2/\kappa$; therefore, Eq. (43) transforms to

$$\begin{aligned}\dot{V}_4 &\le -\frac{k_5 u_i}{\kappa V_i}S_2^2 + \kappa\varepsilon \\ &= -\frac{2k_5 u_i}{\kappa V_i}V_4 + \kappa\varepsilon.\end{aligned} \tag{47}$$

Thus, the value of V_4 at any time can be bounded as follows

$$0 \le V_4(t) \le V_4(0)e^{-\frac{2k_5 u_i}{\kappa V_i}t} + \frac{\kappa^2\varepsilon V_i}{2k_5 u_i}. \tag{48}$$

Under the effect of the control input τ_{ui}, the sliding manifold S_2 will converge to the region of $\{S2||S2| < \kappa\}$ in a finite time and then maintain it. By magnifying k_5 and reducing κ appropriately, the residual convergence error can be minimized to an acceptance range.

Differentiating both sides of Eq. (24) and integrating Eqs. (25), (36), and (46) into it yields

$$\begin{aligned}\dot{V}_2 &\le \sum_{i=1}^{n}\left[-\frac{k_5 u_i}{\kappa V_i}(V_i - V_{id})^2 + \kappa\varepsilon - \lambda_1\lambda_2\theta_i^2 + \lambda_2\theta_i S_2\right] \\ &\le -\sum_{i=1}^{n}\left[\frac{k_5 u_i}{\kappa V_i}(V_i - V_{id})^2 + 4\lambda_1 V_i V_{id}\sin^2(\theta_i/2)\right] \\ &\quad + \sum_{i=1}^{n}(\kappa\varepsilon + \lambda_2|\theta_i S_2|) \le -k\tilde{\boldsymbol{P}}^T\tilde{\boldsymbol{P}} + \rho,\end{aligned} \tag{49}$$

where

$$k = \min\left\{\lambda_1, \frac{k_5 u_1}{\kappa V_1}, \frac{k_5 u_2}{\kappa V_2}, \ldots, \frac{k_5 u_n}{\kappa V_n}\right\}$$

$$\rho = \sum_{i=1}^{n}(\kappa\varepsilon + \lambda_2|\theta_i S_2|).$$

The following Lyapunov function candidate is designed:

$$V_5 = \frac{1}{2}\boldsymbol{e}_h^T\boldsymbol{K}_1\boldsymbol{e}_h + k_3\Phi + V_2. \tag{50}$$

Differentiating both sides of Eq. (51) yields

$$\begin{aligned}\dot{V}_5 &\le -(\boldsymbol{J}_s^T\boldsymbol{K}_1\boldsymbol{e}_h + k_3\boldsymbol{\varphi})^T(\boldsymbol{J}_s^T\boldsymbol{K}_1\boldsymbol{e}_h + k_3\boldsymbol{\varphi}) + (\boldsymbol{J}_s^T\boldsymbol{K}_1\boldsymbol{e}_h + k_3\boldsymbol{\varphi})\tilde{\boldsymbol{P}} \\ &\quad -k\tilde{\boldsymbol{P}}^T\tilde{\boldsymbol{P}} - \boldsymbol{\varphi}^T\boldsymbol{J}_s^+\dot{\boldsymbol{X}}_h + \rho \\ &= -\left(\boldsymbol{J}_s^T\boldsymbol{K}_1\boldsymbol{e}_h + k_3\boldsymbol{\varphi} + \frac{1}{2}\tilde{\boldsymbol{P}}\right)^T\left(\boldsymbol{J}_s^T\boldsymbol{K}_1\boldsymbol{e}_h + k_3\boldsymbol{\varphi} + \frac{1}{2}\tilde{\boldsymbol{P}}\right) \\ &\quad -\left(k - \frac{1}{4}\right)\tilde{\boldsymbol{P}}^T\tilde{\boldsymbol{P}} - \boldsymbol{\varphi}^T\boldsymbol{J}_s^+\dot{\boldsymbol{X}}_h + \rho.\end{aligned} \tag{51}$$

If we make $k > 1/4$, then Eq. (51) can be rewritten as follows:

$$\dot{V}_5 \le -\left(\boldsymbol{J}_s^T\boldsymbol{K}_1\boldsymbol{e}_h + k_3\boldsymbol{\varphi} + \frac{1}{2}\tilde{\boldsymbol{P}}\right)^T\left(\boldsymbol{J}_s^T\boldsymbol{K}_1\boldsymbol{e}_h + k_3\boldsymbol{\varphi} + \frac{1}{2}\tilde{\boldsymbol{P}}\right) + \delta, \tag{52}$$

where $\delta = |\boldsymbol{\varphi}^T\boldsymbol{J}_s^T\dot{\boldsymbol{X}}_h| + \rho$.

Because $\rho, \|\boldsymbol{\varphi}^T\|, \|\dot{\boldsymbol{X}}_h\|$ are bounded and $\|\boldsymbol{\varphi}^T\|$ is irrelevant to $\|\dot{\boldsymbol{X}}_h\|$, δ is also bounded. By selecting appropriate control parameters, $\dot{V}_5$ is a semi-global negative, and the total system $(\boldsymbol{e}_h, \boldsymbol{\varphi}, \tilde{\boldsymbol{P}})$ is asymptotically stable and remains in a compact set after completing obstacle avoidance. Thus, the stability of the controller is proved.

4. Numerical simulations

This section presents numerical simulations of a USV swarm to demonstrate the effectiveness of the proposed control algorithm. The swarm is composed of six USVs that are homogeneous and underactuated along the sway axis. Each USV is equipped with one propeller and one rudder. The motion parameters provided are listed in Table 1.

In the simulations, the control parameters discussed in Section 3 are set as follows: $k_1 = 10$, $k_2 = 5$, $k_3 = 1$, $k_4 = 20$, $k_5 = 20$, $\kappa = 0.5$, $\zeta = 1$, $\omega = 5$, $\lambda_1 = 20$ and $\boldsymbol{K}_1 = diag\{0.5, 0.5, 0.5\}$.

The following simulations include external disturbances to demonstrate that the controller is robust. The disturbances are designed as $\xi_u = 0.2m_{11} \times \mathrm{rand}(1), \xi_v = 0.2m_{22} \times \mathrm{rand}(1)$

Table 1
Ship motion parameters.

$m_{11} = 120 \times 10^3$ kg	$d_u = 215 \times 10^2$ kg s^{-1}	$d_{|u|u} = 0.2d_u$
$m_{22} = 177.9 \times 10^3$ kg	$d_v = 147 \times 10^3$ kg s^{-1}	$d_{|v|v} = 0.2d_v$
$m_{33} = 636 \times 10^5$ kg	$d_r = 802 \times 10^4$ kg s^{-1}	$d_{|r|r} = 0.2d_r$

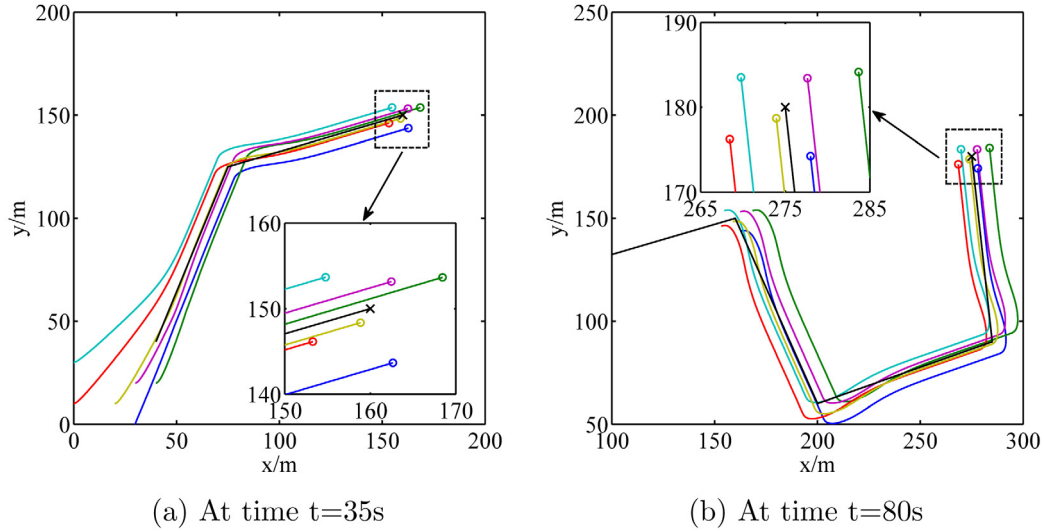

Fig. 5. Tracking path of the swarm.

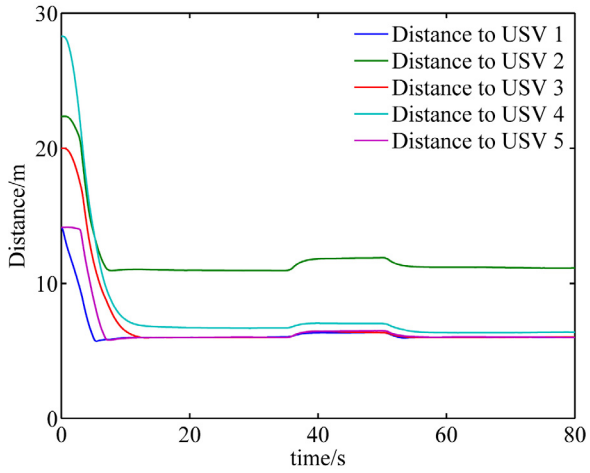

Fig. 6. Distance between USV 6 and other USVs.

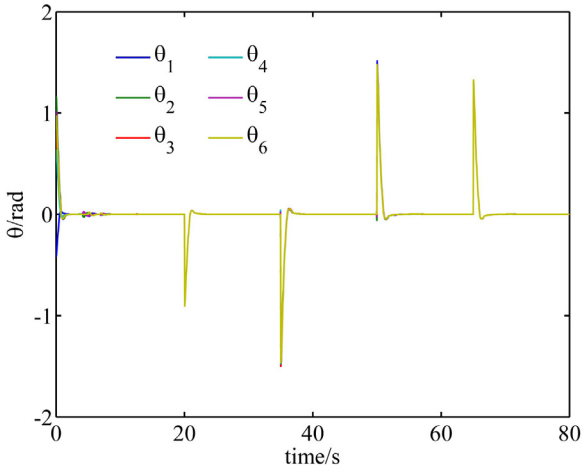

Fig. 8. Error curves of the desired yaw angles.

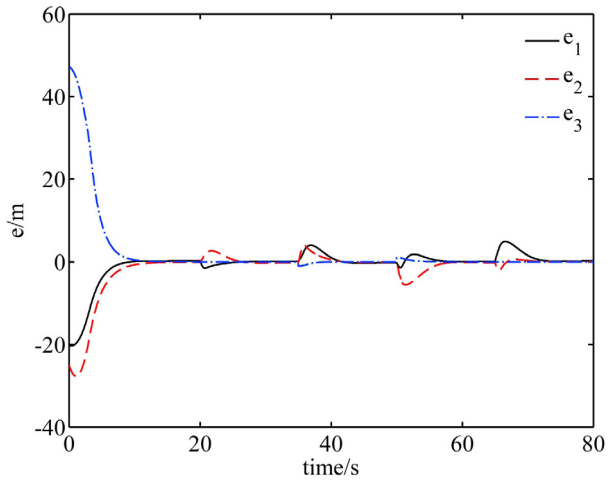

Fig. 7. Error curves of the desired position function.

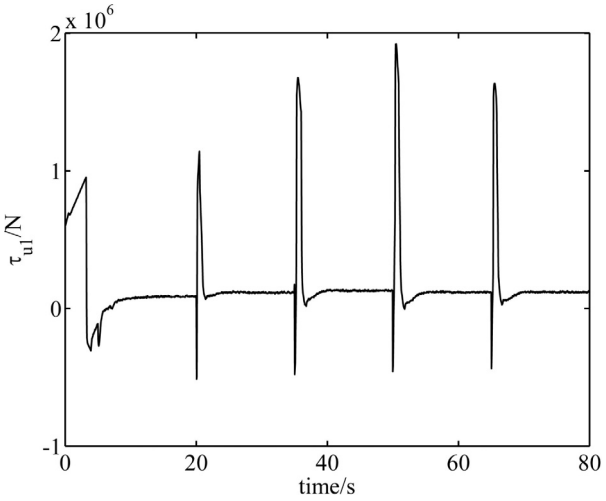

Fig. 9. Surge thrust of the 1st USV.

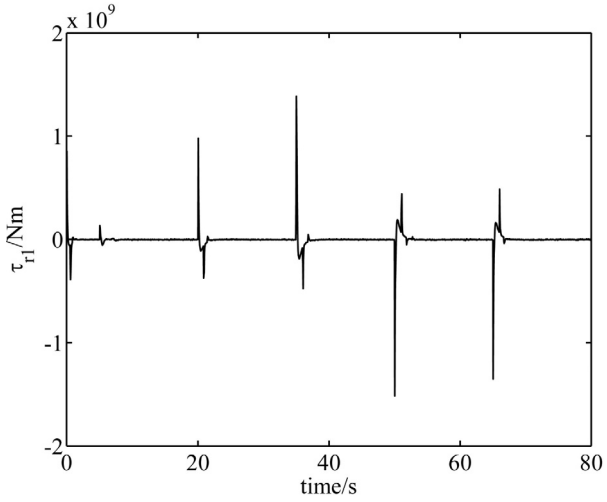

Fig. 10. Yaw moment of the 1st USV.

and $\xi_r = 0.1m_{33} \times \text{rand}(1)$, where rand(1) represents random noise drawn from the standard uniform distribution on the open interval (0,1). Thus, the disturbances are nonzero mean values. While these may differ somewhat from environmental disturbances encountered in practice, such variations should not affect the verification of this controller through these simulations.

4.1. Simulation 1: target tracking without obstacle avoidance

In the first case, the swarm tracks a moving underwater target in open waters in which the target is moving along a polyline. There is no obstacle near the path, but the USVs still need to avoid collisions with each other while tracking the target.

Assume that the position of the target, (x_t, y_t), is always known. Therefore, the desired position function is defined as $\boldsymbol{X}_h = [x_t, y_t, \sigma_d]^T$. For collision avoidance, the max and min safe distances adopted are $R_r = 6$ m, $r_r = 3$ m. The target starts from the point A(40 m,40 m) at time $t = 0$ s and reaches the points B (75 m,125 m), C (160 m,150 m), D (200 m,60 m), E (280 m,90 m), and F (275 m,180 m) at $t = 20$ s, 35 s, 50 s, 65 s, and 80 s, respectively. The target speed is assumed to be constant during each time period. The desired swarm distance variances are set to $\sigma_d = 7$ m at $t = 0$–35 s, 50 s ~ 80 s and $\sigma_d = 8$ m at $t = 35$–50 s. The overall performance of the swarm is illustrated in Figs. 5–10 .

Fig. 5(a) shows the tracking path of the USV swarm at time $t = 35$ s, while (b) shows the tracking path at $t = 80$ s. In both images, the black polyline represents the path of the moving target, and the six colored curves represent the tracking paths of each

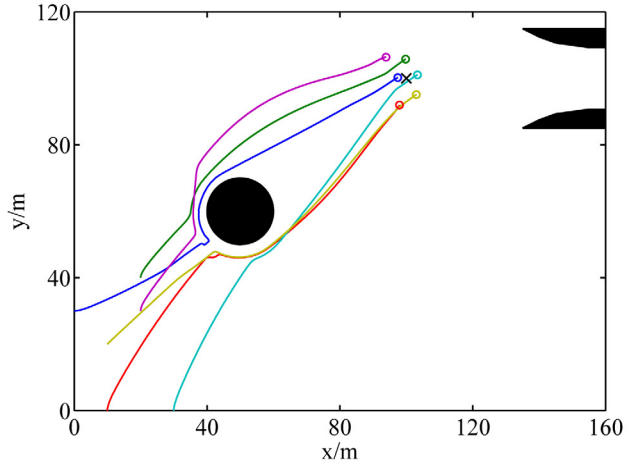

(a) At time t=20s

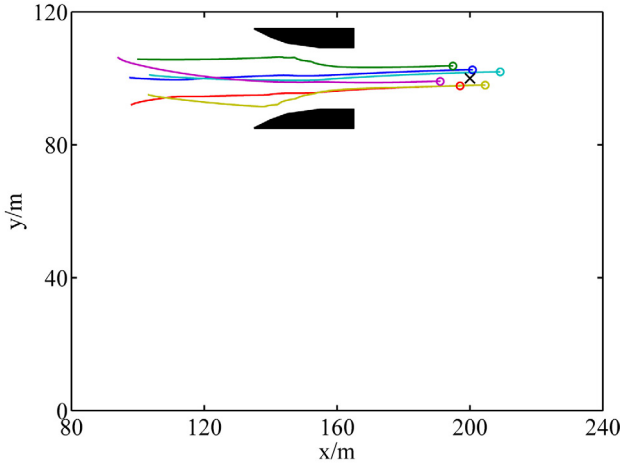

(b) At time t=40s

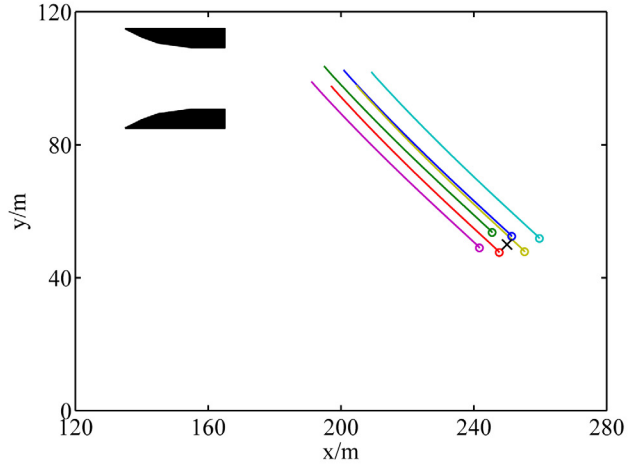

(c) At time t=60s

Fig. 11. Way-point tracking with obstacle avoidance.

individual USV. As shown, each USV tracks the moving target well with an acceptable overshoot at the turning points. Initially, the 6 USVs are well separated, but they converge rapidly to form a relatively stable formation shape while tracking the target. During automatic navigation, the 6 USVs remain a safe distance from each other; no collisions between USVs occurred during this simulation.

For a more comprehensive depiction concerning the collision avoidance of the swarm members, the distances between the 6th USV and other USVs are plotted in Fig. 6. The 6th USV corresponds to the yellow circle in Fig. 5, and it is close to the center of the swarm. At the time periods $t = 10\,\text{s} \sim 35\,\text{s}$ and $t = 50\,\text{s} \sim 80\,\text{s}$, the minimum distance value approaches 6 m because of the potential field effect, in which the maximum safe distance R_r is 6 m. The virtual repulsive forces between USVs achieve the goal of avoiding collisions between swarm members.

Figs. 7 and 8 show error curves for the desired position function and desired yaw angle, respectively. Note that the initial errors are rapidly eliminated. The rebounds at times $t = 20\,\text{s}$, 35 s, 50 s and 65 s are caused by the changes in the target path where the USVs require some time to make a turn. For convenience, only the control inputs of the first USV are illustrated. Figs. 9 and 10 present the surge thrust τ_{u1} and yaw moment τ_{r1}, respectively. Because of the boundary layer function in Eq. (36), the chattering effect does not occur, and the small control input oscillations are caused by non-vanishing disturbances.

From evaluating Figs. 5–9, we can conclude that the proposed methodology and hierarchical control system perform well for tracking a moving target, and the controller is robust.

4.2. Simulation 2: waypoint tracking with obstacles avoidance

In Simulation 2, the USV swarm tracks some waypoints set by the human supervisor when obstacles occur along the route. In this case, the swarm moves toward the target waypoints in sequence.

Based on the positions of the way points, the desired position functions are defined as: $\boldsymbol{X}_h = [100, 100, 8]^T$ at t=0∼20s, $\boldsymbol{X}_h = [200, 100, 8]^T$ at $t = 20$–$40\,\text{s}$ and $\boldsymbol{X}_h = [250, 50, 7]^T$, at $t = 40$–$60\,\text{s}$. As for the obstacles avoidance, the max and min safe distances are set to: $R_o = 20\,\text{m}$, $r_o = 10\,\text{m}$ when the obstacle is rounded or $R_o = 10\,\text{m}$, $r_o = 5\,\text{m}$ when the obstacle is irregular. In this simulation, the control parameters are set the same as for Simulation 1, except for $\boldsymbol{K}_1 = diag\{0.25, 0.25, 0.5\}$.

Fig. 11 shows the sailing paths of the USVs during way-point tracking, and subfigures (a), (b), (c) denote the paths at the time periods $t = 0$–$20\,\text{s}$, $t = 20$–$40\,\text{s}$, and $t = 40$–$60\,\text{s}$, respectively. As Fig. 11(a) shows, when encountering a round obstacle, the 6 USVs opt to abandon the formation shape and bypass the obstacle separately; they reach the first target point (100 m, 100 m) at time $t = 20\,\text{s}$. Note that during swarm members do not collide during obstacle avoidance. In Fig. 11(b), the swarm moves toward the second target point (200 m, 100 m) and must pass through a narrow channel. Under the virtual repulsive forces from the obstacles, the swarm members move closer to the center of the course and transit the channel smoothly. In Fig. 11(c), there are no nearby obstacles; the swarm maintains a stable formation and moves directly to third target point (250 m, 50 m).

Figs. 12 and 13 show the error curves of the desired position function and desired yaw angle, respectively. In Fig. 12, the initial errors converge to zero asymptotically, which means that the swarm reaches the waypoints, gradually obtaining the desired distance variance. Obvious rebounds of e_3 appear in Fig. 12 and θ_i appears in Fig. 13 at the times t=2s and t=22s, which occurs because the collision and obstacle avoidance tasks have a higher priority than the flocking task does, which is reasonable. From Simulation 2, we can conclude that the controller also performs well to avoid collisions in obstacle avoidance situations.

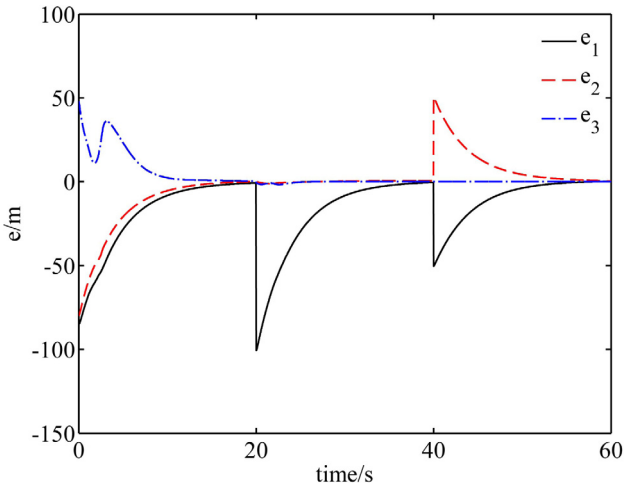

Fig. 12. Error curves of the desired position function.

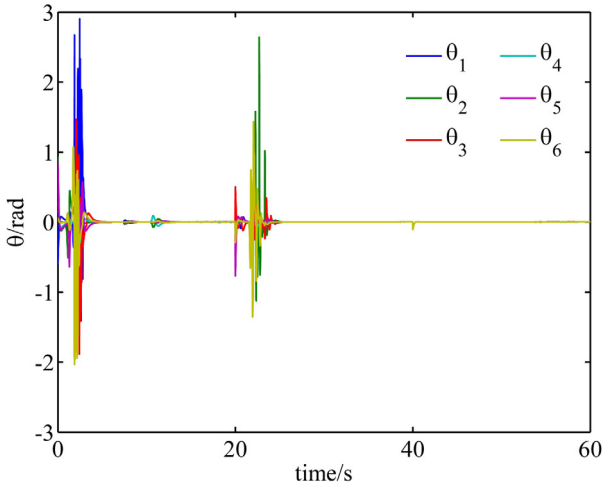

Fig. 13. Error curves of the desired yaw angles.

5. Conclusions and future work

In this paper, a hierarchical control framework with relevant algorithms was proposed to achieve auto navigation of a USV swarm, enabling the swarm to track a desired target, avoid obstacles and avoid collisions between swarm members autonomously. Theoretical proof and numerical simulations are provided to demonstrate that the overall control system is both efficient and robust.

From the simulation results, the designed hierarchical swarm controller based on APF method and individual motion planning is quite suitable for underactuated USV swarms. Compared to formation control methods, the swarm does not need to maintain a fixed formation, and the swarm members are intelligent to a certain extent.

The main contributions of this paper can be considered from three aspects. First, by designing the center position and distance variance based flocking strategy, swarm control studies have been extended from robots with 2 DOF to USVs with 3 DOF. Second, the APF method has been improved in two ways: one creates a velocity related potential function by adding a damping coefficient in formulas, the other is the design of an irregular potential field that can avoid obstacles of any shape. Finally, this paper developed an integrated control framework for autonomous control of USV swarm

that covers control processes from defining a desired position to planning real-time motion and the design of control inputs.

In future work, the proposed method for USV swarm control will be improved by heightening the practicability with which it can be converted to practical use. First, avoidance of moving targets (i.e. sailing ships) will be further studied. Then, an actual electronic chart will be adopted and pixelated to model external geographical information for USVs. Eventually, after the theoretical study is mature and has obtained sufficient financial support, a model-ship USV swarm sailing test will be conducted to demonstrate that the swarm control method can be applied in real-world conditions.

Acknowledgements

We would like to thank the associate editor and the reviewers for their helpful comments. We would also like to thank the Laboratory Foundation of Science and Technology on Water Jet Propulsion (Grant No. 61422230302162223013), the National Natural Science Foundation of China (Grant No. 51409054), and the Fundamental Research Funds for the Central Universities (Grant No. HEUCFJ170106) for their financial support of our research.

References

[1] K.D. Do, Practical formation control of multiple underactuated ships with limited sensing ranges, Robot. Auton. Syst. 59 (6) (2011) 457–471.
[2] J.Y. Zhuang, Y.M. Su, Y.L. Liao, et al., Unmanned surface vehicle local path planning based on marine radar, J. Shanghai Jiaotong Univ. 9 (2012) 006.
[3] K. Shojaei, Neural adaptive robust control of underactuated marine surface vehicles with input saturation, Appl. Ocean Res. 53 (2015) 267–279.
[4] Y. Liu, R. Bucknall, The angle guidance path planning algorithms for unmanned surface vehicle formations by using the fast marching method, Appl. Ocean Res. 59 (2016) 327–344.
[5] R.J. Wai, C.M. Liu, Y.W. Lin, Design of switching path-planning control for obstacle avoidance of mobile robot, J. Frankl. Inst. 348 (4) (2011) 718–737.
[6] R. Cui, S.S. Ge, B.V.E. How, et al., Leaderfollower formation control of underactuated autonomous underwater vehicles, Ocean Eng. 37 (17) (2010) 1491–1502.
[7] Z. Peng, D. Wang, Z. Chen, et al., Adaptive dynamic surface control for formations of autonomous surface vehicles with uncertain dynamics, IEEE Trans. Control Syst. Technol. 21 (2) (2013) 513–520.
[8] L. Ding, G. Guo, Formation control for ship fleet based on backstepping, Control Decis. 27 (2) (2012) 299–303.
[9] H. Mehrjerdi, J. Ghomman, M. Saad, Nonlinear coordination control for a group of mobile robots using a virtual structure, Mechatronics 21 (7) (2011) 1147–1155.
[10] K.D. Do, Formation control of underactuated ships with elliptical shape approximation and limited communication ranges, Automatica 48 (2012) 1380–1388.
[11] T. Glotzbach, M. Schneider, P. Otto, Cooperative line of sight target tracking for heterogenous unmanned marine vehicle teams: from theory to practice, Robot. Auton. Syst. 67 (2015) 53–60.
[12] X. Cai, M. de Queiroz, Adaptive rigidity-based formation control for multi robotic vehicles with dynamics, IEEE Trans. Control Syst. Technol. 23 (1) (2015) 389–396.
[13] V. Gazi, Swarm aggregations using artificial potentials and sliding-mode control, IEEE Trans. Robot. 21 (6) (2005) 1208–1214.
[14] T. Sousselier, J. Dreo, M. Sevaux, Line formation algorithm in a swarm of reactive robots constrained by underwater environment, Expert Syst. Appl. 42 (12) (2015) 5117–5127.
[15] H. Kim, D. Kim, H. Kim, et al., An extended any-angle path planning algorithm for maintaining formation of multi-agent jellyfish elimination robot system, Int. J. Control Autom. Syst. 14 (2) (2016) 598–607.
[16] R. Song, Y. Liu, R. Bucknall, A multi-layered fast marching method for unmanned surface vehicle path planning in a time-variant maritime environment, Ocean Eng. 129 (2017) 301–317.
[17] D.V. Dimarogonas, K.J. Kyriakopoulos, Connectedness preserving distributed swarm aggregation for multiple kinematic robots, IEEE Trans. Robot. 24 (5) (2008) 1213–1223.
[18] L. Sabattini, N. Chopra, C. Secchi, Decentralized connectivity maintenance for cooperative control of mobile robotic systems, Int. J. Robot. Res. 32 (12) (2013) 1411–1423.
[19] Y. Liu, R. Bucknall, Path planning algorithm for unmanned surface vehicle formations in a practical maritime environment, Ocean Eng. 97 (2015) 126–164.
[20] J.T. Johnson, A brief investigation of swarm theory and applications, in: ASME 2009 International Design Engineering Technical Conferences and Computers and Information in Engineering Conference, American Society of Mechanical Engineers, 2009, pp. 209–218.
[21] W. Deng, H. Zhao, J. Liu, et al., An improved CACO algorithm based on adaptive method and multi-variant strategies, Soft Comput. 19 (3) (2015) 701–713.
[22] W. Deng, R. Chen, B. He, et al., A novel two-stage hybrid swarm intelligence optimization algorithms and application, Soft Comput. 16 (10) (2012) 1707–1722.
[23] B. Gu, V.S. Sheng, K.Y. Tay, et al., Incremental support vector learning for ordinal regression, IEEE Trans. Neural Netw. Learn. Syst. 26 (7) (2015) 1403–1416.
[24] B. Gu, V.S. Sheng, A robust regularization path algorithm for v-support vector classification, IEEE Trans. Neural Netw. Learn. Syst. PP (99) (2016) 1–8.
[25] M. Christoph, S. Thomas, C. Karl, A minimalist flocking algorithm for swarm robots Advances in Artificial Life. Darwin Meets von Neuman, Lecture Notes in Computer Science, vol. 5778, 2011, pp. 375–382.
[26] Y. Tan, Z. Zheng, Research advance in swarm robotics, Def. Technol. 9 (2013) 18–39.
[27] Z. Fu, K. Ren, J. Shu, et al., Enabling personalized search over encrypted outsourced data with efficiency improvement, IEEE Trans. Parallel Distrib. Syst. 27 (9) (2016) 2546–2559.
[28] R. Cepeda-Gomez, N. Olgac, D.A. Sierra, Application of sliding mode control to swarms under conflict, in: ASME 2010 Dynamic Systems and Control Conference, American Society of Mechanical Engineers, 2010, pp. 615–622.
[29] Z. Pan, Y. Zhang, S. Kwong, Efficient motion and disparity estimation optimation for low complexity multiview video coding, IEEE Trans. Broadcast. 61 (2) (2015) 166–176.
[30] Y.C. Liu, Task-space coordination control of bilateral humanswarm systems, J. Frankl. Inst. 352 (1) (2015) 311–331.
[31] L.E. Barnes, M.A. Fields, K.P. Valavanis, Swarm formation control utilizing elliptical surface and limiting functions, IEEE Trans. Syst. Man Cybern. Part B (Cybern.) 39 (6) (2009) 1434–1445.
[32] S. Hettiarechchi, W.M. Spears, Distributed adaptive swarm for obstacle avoidance, Int. J. Intell. Comput. Cybern. 2 (4) (2009) 644–671.
[33] S. Etemadi, A. Alasty, G.R. Vossoughi, Stability analysis of robotic swarm with limited field of view, in: ASME 2007 International Mechanical Engineering Congress and Exposition, American Society of Mechanical Engineers, 2007, pp. 175–184.
[34] A. Franchi, C. Secchi, H.I. Son, et al., Bilateral teleoperation of groups of mobile robots with time-varying topology, IEEE Trans. Robot. 28 (5) (2012) 1019–1033.
[35] K.D. Do, Practical control of underactuated ships, Ocean Eng. 37 (13) (2010) 1111–1119.
[36] Y. Liao, M. Zhang, L. Wan, Serret-Frenet frame based on path following control for underactuated unmanned surface vehicles with dynamic uncertainties, J. Cent. South Univ. 22 (2015) 214–223.
[37] Y.C. Liu, N. Chopra, Controlled synchronization of heterogeneous robotic manipulators in the task space, IEEE Trans. Robot. 28 (1) (2012) 268–275, 214–223.
[38] D.M. Stipanovi, P.F. Hokayem, M.W. Spong, et al., Cooperative avoidance control for multiagent systems, J. Dyn. Syst. Meas. Control 129 (5) (2007) 699–707.
[39] L.P. Perera, C.G. Soares, Pre-filtered sliding mode control for nonlinear ship steering associated with disturbances, Ocean Eng. 51 (2012) 49–62.
[40] Z. Qin, L. Zhuang, P. Li, et al., Sliding-mode control of path following for underactuated ships based on high gain observer, J. Cent. South Univ. 23 (12) (2016) 3356–3364.
[41] Y. Yang, G. Xia, Path-following in 3d for underactuated autonomous underwater vehicle based on ocean-current observer, Control Theory Appl. 8 (30) (2013) 974–980.
[42] W. Yan, Research on Nonlinear Robust Control of Underactuated Surface Vessels Motion, Herbin Engineering University, Herbin, 2013, pp. 56–70.